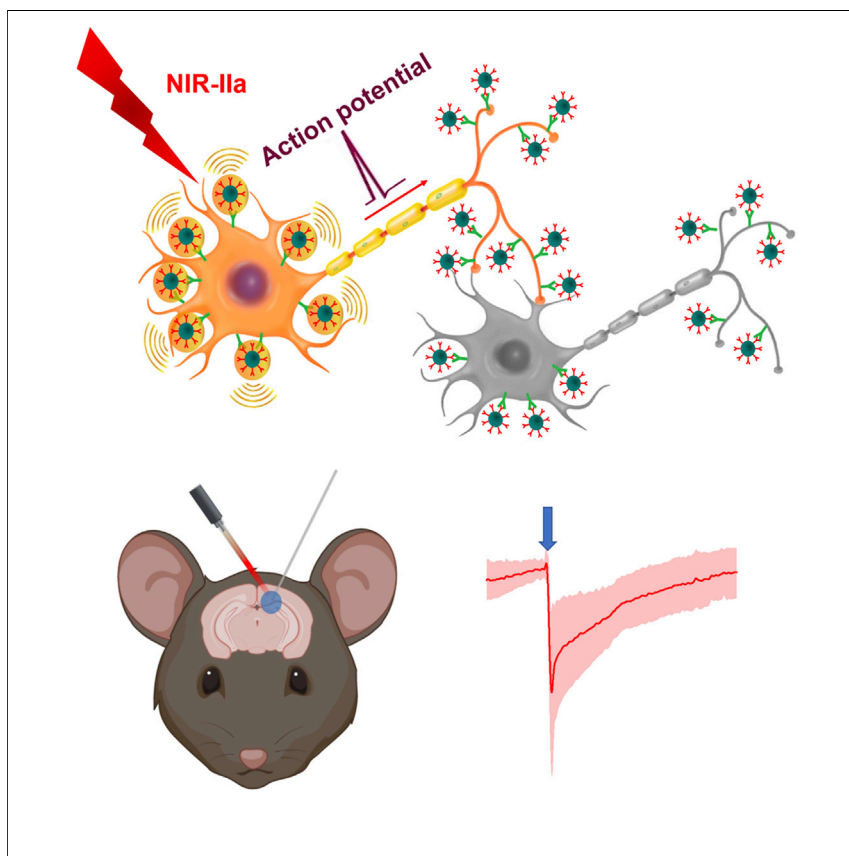


Article

Neural Stimulation *In Vitro* and *In Vivo* by Photoacoustic Nanotransducers

Ying Jiang, Yimin Huang, Xuyi Luo, ..., Heng-Ye Man, Ji-Xin Cheng, Chen Yang

cheyang@bu.edu

HIGHLIGHTS

Non-genetic neural stimulation using photoacoustic nanoparticles is reported

Nanotransducers generate photoacoustic signals upon 1,030-nm nanosecond laser excitation

Nanotransducer stimulation targets a mechanosensitive channel on neuron membrane

Single-cell stimulation through nanotransducers is reported

Neuromodulation is crucial for the understanding of brain circuits and treatment of neurological diseases. This work demonstrates a new photoacoustic nanoparticle-based neural stimulation technique. Synthesized nanoparticles transduce near-infrared light to ultrasound locally at the neuronal membrane and evoke neural activation *in vitro* and *in vivo*. Through targeting the mechanosensitive ion channel TRPV4, the modified nanotransducers achieve neural activation with enhanced specificity. Together, photoacoustic nanotransducers offer opportunities for non-genetic neuromodulation with deep tissue penetration.

**Development**

Practical, real world, technological considerations and constraints

Jiang et al., Matter 4, 654–674
February 3, 2021 © 2020 Elsevier Inc.
<https://doi.org/10.1016/j.matt.2020.11.019>



Article

Neural Stimulation *In Vitro* and *In Vivo* by Photoacoustic Nanotransducers

Ying Jiang,^{1,9} Yimin Huang,^{2,9} Xuyi Luo,³ Jiayingzi Wu,³ Haonan Zong,⁴ Linli Shi,² Ran Cheng,² Yifan Zhu,⁴ Shan Jiang,⁵ Lu Lan,⁴ Xiaoting Jia,⁵ Jianguo Mei,³ Heng-Ye Man,^{6,7} Ji-Xin Cheng,^{4,8} and Chen Yang^{2,4,10,*}

SUMMARY

Neuromodulation is an invaluable approach for the study of neural circuits and clinical treatment of neurological diseases. Here, we report semiconducting polymer nanoparticles based photoacoustic nanotransducers (PANs) for neural stimulation *in vitro* and *in vivo*. Our PANs strongly absorb the nanosecond pulsed laser in the near-infrared second window (NIR-II) and generate localized acoustic waves. PANs are shown to be surface modified and selectively bind onto neurons. PAN-mediated activation of primary neurons *in vitro* is achieved with ten 3-ns laser pulses at 1,030 nm over a 3-ms duration. *In vivo* neural modulation of mouse brain activities and motor activities is demonstrated by PANs directly injected into brain cortex. With submillimeter spatial resolution and negligible heat deposition, PAN stimulation is a new non-genetic method for precise control of neuronal activities, opening up potentials in non-invasive brain modulation.

INTRODUCTION

Neural stimulation is an important tool enabling our understanding of how brains function and treatments of neurological disorders. Electrical stimulation is the basis of current implantable devices and has already been used in the clinical treatment of depression, Parkinson's disease, and Alzheimer's disease. These devices, often made of metal electrodes, are limited by their invasive nature,¹ inability to target precisely due to current spread, and magnetic resonance imaging incompatibility. Non-invasive clinical or preclinical methods, such as transcranial magnetic stimulation² and transcranial direct current stimulation,³ do not require a surgical procedure but offer a spatial resolution on the order of several millimeters. Optogenetics has been shown to be a powerful method for modulating population neural activities in rodents more precisely and with cell specificity.^{4,5} Optogenetics requires genetic modification through viral infection, which makes it challenging to be applied to humans.⁶ Ultrasound neuromodulation, an emerging non-invasive neuromodulation method, has been demonstrated to evoke action potentials *in vitro* and behavioral responses *in vivo* in rodents,^{7,8} non-human primates,⁹ and even in human subjects.^{10–13} However, the spatial resolution for conventional ultrasound neuromodulation is still limited to several millimeters. More recently, a fiber-based optoacoustic converter has been proposed and demonstrated to achieve neuromodulation with submillimeter spatial resolution utilizing the optoacoustic effect,¹⁴ although it requires surgical implantation for *in vivo* applications.

Nanostructures target neuron membrane locally and convert and amplify the external excitation to local stimuli, offering new interfaces as promising alternative

Progress and Potential

Precise neuromodulation is critical to understanding how the brain functions under healthy and diseased conditions. In this work, we introduce the photoacoustic nanoparticles (PANs) that generate acoustic waves locally on the neuronal membrane. Non-genetic neural stimulation was achieved both *in vitro* and *in vivo* with nanosecond laser excitation in the near-infrared second window (NIR-II). Specificity of the stimulation was further improved by targeting of mechanosensitive TRPV4 channels on the neuronal membrane. With its unique absorption in the NIR-II and the absence of genetic modification, PANs open up the potential for non-invasive neuromodulation with high spatial resolution in deep tissue for rodents as well as primates and humans.

neural stimulation approaches. Gold nanoparticles and nanorods have been studied for photothermal neural stimulation *in vitro*.^{15–18} Gold nanoparticles and carbon nanotubes have also been used for photothermal-driven optocapacitive stimulation *in vitro*.^{19–21} The Tian and Bezanilla groups reported photoelectrical stimulations with silicon nanostructures.²² In these light-driven stimulations, the wavelengths used were mostly in the range of 520–808 nm, which has limited penetration through skulls and brain tissue. In pursuit of deeper penetration, thermal stimulation triggered by nanoparticles absorbing longer-wavelength light or magnetic field has also been investigated. The Pu group demonstrated photothermal neural stimulation *in vitro* using bioconjugated polymer nanoparticles absorbing 808 nm and binding to transient receptor potential cation channel subfamily V member 1 (TRPV1).^{23,24} The Anikeeva group used gene transfection to overexpress the thermally sensitive ion channels in TRPV1 and then utilized the magnetothermal effect of the paramagnetic nanoparticles to activate these channels.²⁵ In these studies, significant local temperature rise, exceeding the thermal threshold of the ion channels, e.g., 43°C in the case of TRPV 1, for a period longer than several seconds was observed, thus raising concerns over the safety of thermally activated neural stimulation. The Khizroev group used the magnetoelectric nanoparticles under an applied magnetic field to perturb the voltage-sensitive ion channels for neuron modulation.²⁶ Notably, these magnetic stimuli-based techniques deliver a spatial precision relying on the confinement of the magnetic field, which is on the millimeter-to-centimeter scale. New technologies and concepts are still sought to achieve non-invasive, genetic free and precise neural stimulation.

Here, we report the development and application of photoacoustic nanotransducers (PANs) to enable non-genetic neural stimulation in cultured primary neurons and in mouse brain *in vivo* (Figure 1A). Our PANs, based on synthesized semiconducting polymer nanoparticles, efficiently generate localized ultrasound by a photoacoustic process upon absorption of nanosecond pulsed light in the near-infrared second window (NIR-II; 1,000–1,700 nm) (Figure 1B). NIR-II light has the capability of centimeter-deep tissue penetration,^{27,28} which is beyond the reach of visible light currently used in optogenetics. We modified the PAN surface for non-specific binding to neuronal membrane and specific targeting of mechanosensitive ion channels, respectively. We showed that upon excitation at 1,030 nm, PANs on the neuronal membrane successfully activated rat cortical neurons, confirmed by real-time fluorescence imaging of the fluorescent calcium indicator GCaMP6f. The spatial resolution of the PAN stimulation was shown to be completely determined by the illumination area of the light, and single-neuron stimulation was demonstrated under excitation of NIR-II light delivered by a tapered fiber. We then demonstrated *in vivo* motor cortex activation and evoked subsequent motor responses through PANs directly injected into a mouse living brain. Importantly, the heat generated by the nanosecond laser pulses is confined inside the PAN, resulting in a transient temperature rise during the photoacoustic process, evidenced by finite element modeling simulations. Collectively, our findings propose PANs as a new platform for modulating neuronal activities. Triggered by NIR-II light and showing negligible temperature increase, PANs open up opportunities for deep-penetrating-light controlled neural activation with high precision.

RESULTS

Synthesis of PANs

We first synthesized NIR-II absorbing semiconducting polymer bis-isoidigo-based polymer (BTII).²⁹ To obtain nanoparticles and modified the polymer with

¹Graduate Program for Neuroscience, Boston University, Boston, MA 02215, USA

²Department of Chemistry, Boston University, Boston, MA 02215, USA

³Department of Chemistry, Purdue University, West Lafayette, IN 47906, USA

⁴Department of Electrical & Computer Engineering, Boston University, Boston MA 02215, USA

⁵Bradley Department of Electrical and Computer Engineering, Virginia Tech, Blacksburg, VA 24061, USA

⁶Department of Biology, Boston University, Boston, MA 02215, USA

⁷Center for Systems Neuroscience, Boston University, Boston, MA 02215, USA

⁸Department of Biomedical Engineering, Boston University, Boston, MA 02215, USA

⁹These authors contributed equally

¹⁰Lead Contact

*Correspondence: cheyang@bu.edu
<https://doi.org/10.1016/j.matt.2020.11.019>

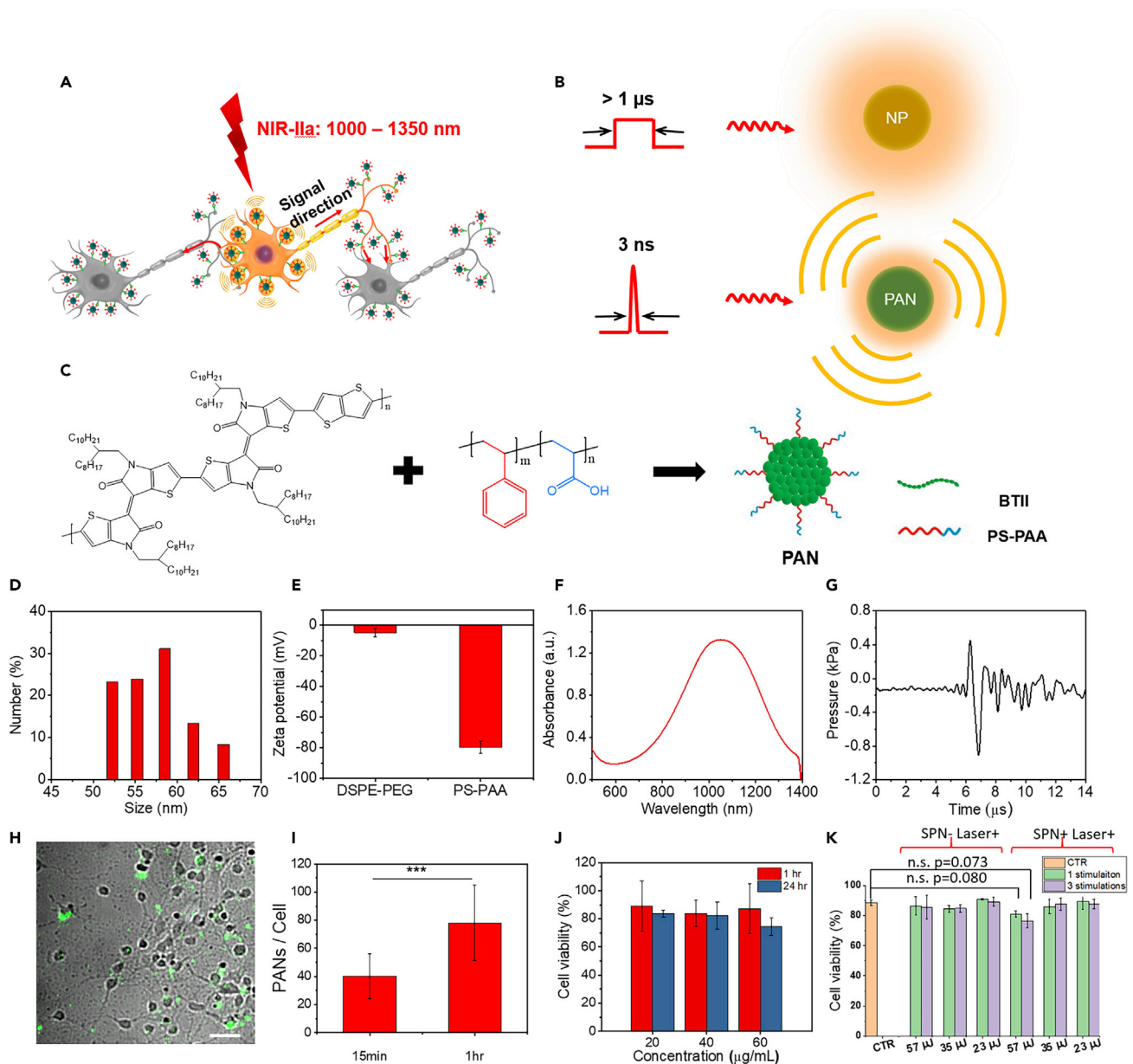


Figure 1. Surface-Modified PANs Sufficiently Bind to Neurons

(A) Scheme of the PAN-induced neural stimulation.

(B) Schematic illustrating that upon nanosecond laser pulse excitation, a PAN generates photoacoustic signals. NP, nanoparticle.

(C) Schematic of PAN synthesis. BTII, bis-isoindigo-based polymer.

(D) Dynamic light scattering (DLS) analysis of PAN solutions.

(E) Zeta-potential measurement of PAN solutions with a concentration of 1.0 mg/mL with DSPE-PEG and PS-PAA functionalization, respectively.

(F) UV-vis spectrum of PAN solution with a concentration of 1.0 mg/mL.

(G) Photoacoustic signal measured from PAN solution (1.0 mg/mL).

(H) TA images of PANs binding to neurons after 15-min culture. Green, TA channel; gray, transmission channel. Scale bar, 50 μm.

(I) Binding density analysis of PANs to soma regions of neurons at 15 min and 1 h, respectively.

(J) Cytotoxicity analysis of PANs to neurons by MTT assay.

(K) Cell viability assay for neurons treated with PAN and laser excitation (one stimulation and three stimulations) and treated with laser excitation only (CTR).

Data are presented as mean ± SD. Two-sample t test: n.s., not significant ($p > 0.5$); *** $p < 0.001$.

polystyrene-block-poly(acryl acid) (PS-b-PAA) via a nanoprecipitation method (Figure 1C). The PS-b-PAA was chosen due to the amphiphilic nature of its chemical structure. The hydrophobic polystyrene portion forms a π - π stacking with the polymer, while the hydrophilic poly(acryl acid) (PAA) makes the polymer into water-soluble nanoparticles with carboxyl groups decorated on the surface. The Fourier transform infrared (FTIR) spectrum confirmed the presence of carboxyl groups (Figure S1), indicating the successful modification. The PANs were dispersed in aqueous solution for characterization. The size of nanoparticles prepared was measured to be 58.0 ± 5.2 nm using dynamic light scattering (DLS) (Figure 1D). Transmission electron microscopy (TEM) imaging of PANs (Figure S2) shows an average particle diameter of 52.9 ± 12.2 nm, consistent with the DLS measurement results. The nanoparticles were found to be negatively charged, indicated by a potential of -79.79 ± 4.04 mV through the zeta-potential measurement. To confirm that the surface negative charge is introduced by the surfactant PS-b-PAA, we performed surface modification using 1,2-distearoyl-*sn*-glycero-3-phosphoethanolamine-*N*-(polyethylene glycol)-2000 (DSPE-PEG), a neutrally charged surfactant, as a comparison. DSPE-PEG-modified PANs were found to be charged with -4.88 ± 3.06 mV (Figure 1E).

PANs Generate Strong Acoustic Waves under NIR-II Light Pulses

The planar backbone of the semiconducting polymer chain pushed the absorption to the NIR-II.³⁰ We confirmed this by UV-visible NIR spectroscopy. The nanoparticles broadly absorb NIR-II light from 800 to 1,300 nm with a peak at 1,100 nm (Figure 1F). Next, we tested whether PANs can generate sufficient optoacoustic waves. In the optoacoustic process, an optoacoustic wave is generated following a transient temperature increase and thermal expansion of the nanoparticle. Importantly, two conditions, stress confinement and thermal confinement, need to be met for efficient photoacoustic generation. The initial pressure p_0 generated is related to light absorption by the following expression: $p_0 = \Gamma \mu_a F$, where μ_a is the absorption coefficient of the absorber, F is the local light fluence, and Γ is the Grüneisen parameter. The Grüneisen parameter can be expressed as $\Gamma = \beta v_s^2 / C_p = \beta / (\kappa \rho C_p)$, where β is the isobaric volume expansion coefficient, C_p is the heat capacity, v_s is the acoustic speed, κ is the isothermal compressibility, and ρ is the mass density.³¹ For the stress confinement, to build up the thermoelastic pressure within a nanoparticle with a diameter of less than 100 nm, considering the speed of sound, a laser pulse of less than 67 ps is required. Yet a mode-locked picosecond pulsed laser usually has several orders of magnitude lower pulse energy than a Q-switched nanosecond pulsed laser. Therefore, nanosecond pulsed lasers are widely used for photoacoustic applications. Regarding thermal confinement, the thermal conduction time must be longer than the laser excitation pulse width to generate photoacoustic waves efficiently. The thermal conduction time can be approximated by $\tau_{th} = L^2 / 4D$, where L is the length of diffusion and D is the thermal diffusivity of local environment. In the case of PAN, the local environment is water around the cell body. Water has a thermal diffusivity of 1.4×10^{-3} cm²/s, and the thermal diffusion length is approximated by the nanoparticle size, which is ~60 nm. The thermal diffusion time constant τ_{th} is thus approximately 6 ns. Therefore, we utilized a nanosecond laser pulse of 3 ns to achieve efficient photoacoustic generation. Measured with an ultrasound transducer with a central frequency at 5 MHz, 1.0 mg/mL nanoparticle solution exhibits a photoacoustic signal showing a waveform in time domain of approximately 2 μ s in width and a peak-to-peak amplitude of 33.95 mV (Figure 1G), under 1,030-nm nanosecond laser with a pulse width of 3 ns, a repetition rate of 3.3 kHz, and an energy density of 21 mJ/cm². The peak pressure was measured to be 1.36 kPa using a needle hydrophone. Since these nanoparticles generate a strong photoacoustic

signal under pulsed NIR-II light, we termed them “photoacoustic nanotransducers” (PANs) and studied their potential for neural binding and stimulation, as detailed below.

PANs Sufficiently Bind to Neurons

As recently reported, nanoparticles with negatively charged surface can bind onto neuronal membrane, whereas positive nanostructures showed no interactions with neurons.³² To examine whether negatively charged PANs can bind onto the neuron membrane, we cultured PANs with embryonic cortical neurons collected from Sprague-Dawley rats. The neurons were first cultured for 15–18 days (days *in vitro*, DIV 15–18). We then added 150 μL of 20 $\mu\text{g}/\text{mL}$ PAN solution into the culture, reaching a concentration of 2 $\mu\text{g}/\text{mL}$. The same concentration was used in all experiments in this work unless otherwise noted.

Confirming and quantifying the binding of PANs to neurons is critical for successful stimulation. Since the semiconducting polymer shows strong intrinsic transient absorption (TA) signals, we then used label-free TA microscopy to visualize binding of PANs to neurons. In TA microscopy, two synchronized femtosecond laser pulse trains, pump and probe respectively, are focused onto the sample. The electronically resonant pump laser pulse excites the molecule to its excited state, after which the probe laser pulse probes the TA change induced by the pump. Such non-linear absorption signals originate from the signature excited state dynamics of the molecule.^{33–36} With outstanding chemical specificity, TA microscopy has been applied to visualize molecular content in biological samples^{37–40} as well as characterization of nanomaterials^{41–46} including semiconducting polymer nanoparticles.^{47,48} Specifically, we used 200-fs laser pulses at 1,045 nm and 845 nm as the pump and probe beams, respectively, with laser power fixed at 20 mW for both beams for TA imaging. To quantify the effective density of PANs bound to neurons, we first measured the signal-to-noise ratio (SNR) of the TA signals of PAN solutions with concentrations ranging from 2.0 to 55.0 $\mu\text{g}/\text{mL}$ to obtain a TA calibration curve (Figure S3). The SNR of TA signals was found to be linear to the PAN concentration with a slope of 14.24 $\text{mL}/\mu\text{g}$. Next, we incubated neurons in culture supplemented with PANs for 15 min, rinsed three times with PBS to remove unbound PANs, and fixed the cells for TA imaging. The PANs were found to bind onto the neurons at an estimated density of 40.2 ± 15.9 PANs per soma (Figure 1H). The number of PANs was calculated on the basis of effective TA concentration estimated according to the measured TA intensity and TA calibration curve, focused spot volume, and estimated molecular weight of PANs. Through depth-resolved TA imaging, the PANs were found to bind mainly on the neuronal membrane instead of entering the neuron through endocytosis (Figure S4). By increasing the culture time to 1 h, a higher binding density was achieved and the number of PANs per neuron on the soma area was found to be 78.1 ± 26.7 (Figures S5 and 1I). In aqueous solution, the PANs prepared show no aggregation. Based on the TA images of PANs co-cultured with neurons, some clusters of PANs were observed when binding to the membranes, possibly due to the complex cellular membrane environment. Different from TA image taken at 15 min co-culture, depth-resolved TA imaging performed at 3 h after PAN addition reveals strong TA signal from PANs located in the cytoplasm, which indicates endocytosis of PANs into the soma (Figure S6).

To test the cytotoxicity of PANs, we performed an MTT (3-(4,5-dimethylthiazol-2-yl)-2,5-diphenyltetrazolium bromide) assay on cultured neurons (DIV 15–18) following incubation with PANs for 1 h and 24 h, respectively. Cell viabilities over 80% were observed in all experimental groups with PAN concentrations ranging from 20 to

60 $\mu\text{g}/\text{mL}$ (Figure 1J), indicating low toxicity of PANs to neurons. To further test whether laser excitation introduces cellular damage and to determine the damage threshold for *in vitro* neural stimulation, we also performed a cell viability assay after laser application with SYTOX Green staining of nuclei.⁴⁹ Neuron cultures at DIV 15–18 were incubated with 150 μL of 20 $\mu\text{g}/\text{mL}$ PAN solution for 15 min. Nanosecond laser at 1,030 nm was delivered to the culture via a 200- μm diameter optical fiber with 0.22 numerical aperture (NA). Conditions of the pulsed laser include a pulse width of 3 ns, a repetition rate of 3.3 kHz, and a laser train of 3 ms (corresponding to 10 laser pulses). As shown in Figure 1K, 1 h after laser excitation, only neurons exposed to 57- μJ laser pulses showed slightly decreased viability, while neurons exposed to laser pulses of 35 and 23 μJ showed similar viability compared with neurons without PAN and laser exposure. Thus, we chose a laser pulse energy of 17 $\mu\text{J}/\text{pulse}$ (pulse energy density of 2.1 mJ/cm^2) for future stimulation experiments. The laser energy chosen is well below the damage threshold from the viability assay as well as American National Standards Institute standard for maximum permissible skin exposure (80 mJ/cm^2 per pulse). These results collectively show that negatively charged PANs can sufficiently bind onto neuronal membranes via a charge-charge interaction, without obvious cytotoxicity upon desired laser excitation.

PANs Stimulate Primary Neurons in Culture

After showing that PANs bind to neurons, we further investigated their potential for neural stimulation. Calcium imaging was performed on Sprague-Dawley rat primary cortical neurons transfected with GCaMP6f on an in-house built wide-field fluorescence microscope. Imaging was performed on five culture batches for each group. Data from a total of 60 neurons, all of which were within 100 μm proximity to the surface of the fiber, were analyzed. The chosen distance of 100 μm was based on the estimated illumination area of the optical fiber. A representative fluorescence image of the neuron culture is shown in Figure 2A, with the dashed circle showing the position of the fiber. Increase in fluorescence intensity of GCaMP6f at individual neurons was clearly observed immediately after applying pulsed laser, as shown in the real-time video (Video S1). Out of the 60 neurons studied, 37 showed an increase in fluorescence greater than 10% or F/F_0 ratio above 1.10 after the laser onset (Figure 2B). F_0 is the baseline fluorescence signal of the neurons before the stimulation. Notably, two types of responses were detected, a transient response shown in Figure 2C and a prolonged response taking a longer time (up to 60 s) to recover to the baseline shown in Figures 2D and S7. We fitted the decay of the response curves exponentially and defined a time constant when they decreased by a factor of $1/e$ ($e = 0.368$) from the peak fluorescence intensity. The transient activations typically show decay time constants ranging from 2 to 5 s, while the prolonged activations have time constants of 5 s and upward (Figure S8). The success rate, defined as the percentage of activated neurons identified through the F/F_0 ratio above 1.10, was calculated. Under the 3-ms laser pulse train, $62.5\% \pm 21.3\%$ of the neurons exhibited activations immediately after the nanosecond laser onset. Specifically, $11.2\% \pm 4.8\%$ and $51.3\% \pm 16.5\%$ were observed as the transient responses and prolonged responses, respectively (Figure 2H).

To investigate whether the activations observed based on the increased fluorescence intensity are caused by action potential, we performed a control experiment with addition of 3 μM tetrodotoxin (TTX), a blocker of voltage-gated sodium channels. After addition of TTX, only a total of 6.7% neurons showed activation upon laser excitation, with $1.7\% \pm 2.9\%$ for transient activation and $5.0\% \pm 5.0\%$ for prolonged activation (Figure 2E), indicating that the observed calcium transients were induced by firing of action potentials. As an additional control, only applying

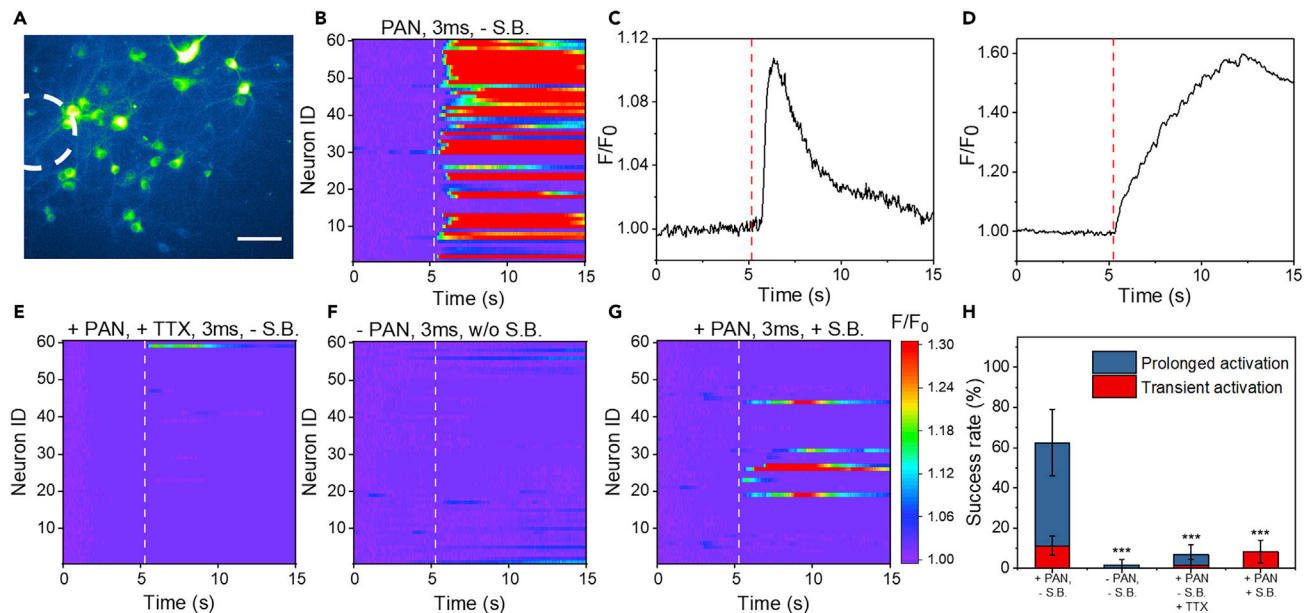


Figure 2. PANs Induce Neural Stimulation

(A) Representative fluorescence image of GCaMP6f-labeled neurons (DIV 15–18) cultured with PANs for 15 min. White dashed line indicates the position of the optical fiber delivering nanosecond pulsed light. Scale bar, 100 μ m.

(B) Colormaps of fluorescence changes of neurons stimulated by PANs using the 1,030-nm nanosecond laser with a 3-ms laser pulse train. White dashed lines indicate laser onsets.

(C and D) Representative fluorescence changes as a function of time for transient activation (C) and prolonged activation (D), respectively. Red dashed lines indicate that laser is on.

(E–G) Colormaps of fluorescence changes of neurons treated with TTX added into the culture medium (E), with laser only (F), and with the synaptic blocker cocktail added in the culture medium (G). Same laser conditions as for (C) and (D) were used. All colormaps were plotted under the same dynamic range.

(H) Success rate analysis. Error bars denote mean \pm SD. p value was calculated using PANs without S.B. group as reference. ***p < 0.001.

nanosecond laser at the same laser condition without PANs induced activation with a success rate of $1.7\% \pm 2.9\%$, indicating that optical excitation through nanosecond laser alone triggers negligible activities (Figure 2F). To investigate how synaptic inputs affects stimulation outcome, we applied a cocktail of synaptic blockers (10 μ M NBQX, 10 μ M gabazine, and 50 μ M DL-AP5)⁵⁰ and observed an overall success rate of $8.3\% \pm 5.8\%$, a significant reduction from 62.5%. Interestingly, the remaining activation is dominantly transient activation, while prolonged activation is completely blocked by the cocktail. These results suggest that the transient activation is likely the result of direct PAN-mediated stimulation, while the prolonged activation comes from a train of action potentials resulting from the activation of neural networks by synaptic transmission. Collectively, the results indicate that PAN-triggered neural activities are action-potential dependent and involve synaptic transmission.

Notably, no activations were found outside the illumination area of the optical fiber (Figures 3A and 3B). Aiming to achieve neural stimulation at single-neuron precision, we applied a tapered optical fiber with a tip diameter of ~ 10 μ m, placed close to the neuron of interest (Figures 3C and 3D). Upon light illumination, only the targeted neuron showed strong calcium activation while other neurons in the field of view remained unchanged. These results indicate that the spatial resolution of PAN stimulation is defined by the illumination of the pulsed light, which makes it possible to achieve neural stimulation at optical resolution through focusing of excitation light.

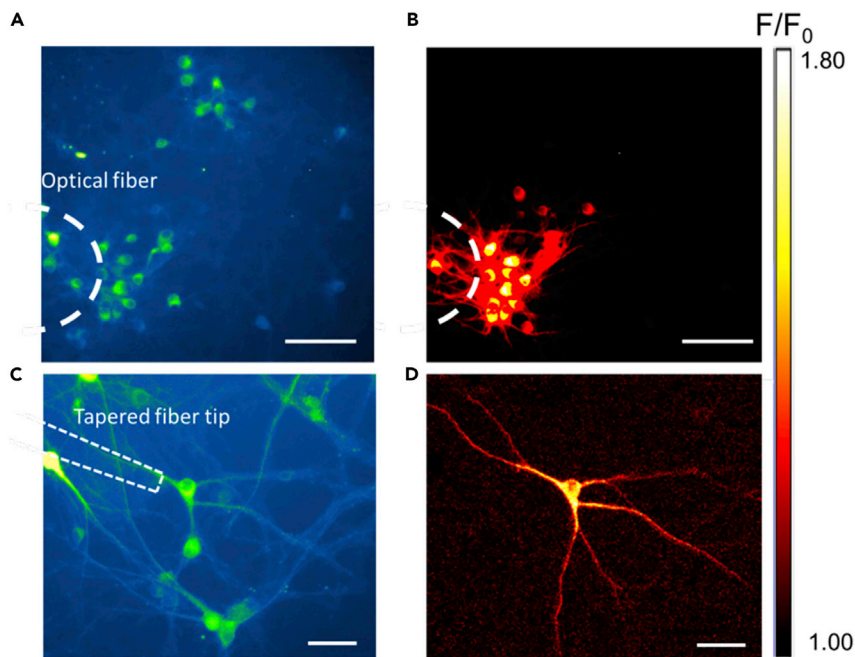


Figure 3. Spatial Distribution of Neuron Activation Induced by PANs

(A) Fluorescence images of neurons before stimulation. Green denotes GCaMP6f. Scale bar, 100 μm .
(B) Maximum $\Delta F/F_0$ image of the field of view after PAN stimulation. Scale bar, 100 μm .
(C) Single-neuron targeting with tapered fiber. Green denotes GCaMP6f. The dashed line indicates the position of the tapered optical fiber tip. Scale bar, 20 μm .
(D) Maximum $\Delta F/F_0$ image of the field of view after PAN stimulation. Scale bar, 20 μm .

Key parameters to control the stimulation through PANs include laser conditions and binding density of PANs on neurons. To understand the effect of the pulsed laser train on activations by PANs, we first studied the activation under increased laser pulse train of 5 and 10 ms, corresponding to 17 and 33 laser pulses, respectively. In the laser only groups, the overall success rate was found to be $3.3\% \pm 2.0\%$ using 5 ms and $18.3\% \pm 10.4\%$ for 10 ms ($n = 60$, three different culture batches), dominated by the prolonged activation (Figures S9A–S9C). With PANs cultured for 15 min with neurons, under the 5-ms laser duration an overall success rate of $66.7\% \pm 14.4\%$ was observed ($n = 60$, three different culture batches). When the laser pulse train increased to 10 ms, the total success rate was found to be $80.0\% \pm 15.3\%$ (Figures S9D–S9F). Notably, both 5-ms and 10-ms laser pulse trains produced neural activities dominated by prolonged activation. The 3-ms pulse train sufficiently produced a high success rate in direct activation with less network effect. Therefore, we identified it as the optimal laser pulse train for PAN-mediated neural stimulation for subsequent experiments.

To investigate how the binding density affects PAN-mediated stimulation, we varied the incubation time of PANs with neuron cultures. In the group where the stimulation was performed immediately after addition of PANs followed with rinses, no neural activation was detected (Figure S10A). This observation confirmed that only bound PANs can trigger the activation. In the group where the stimulation was performed after PANs were incubated with neurons for 1 h, $20.0\% \pm 18.0\%$ of neurons exhibited transient activations and $28.33\% \pm 16.07\%$ exhibited prolonged activation (Figures S10B and S10C). These results indicate that 15-min culture time provides a binding density sufficient to trigger neural stimulation.

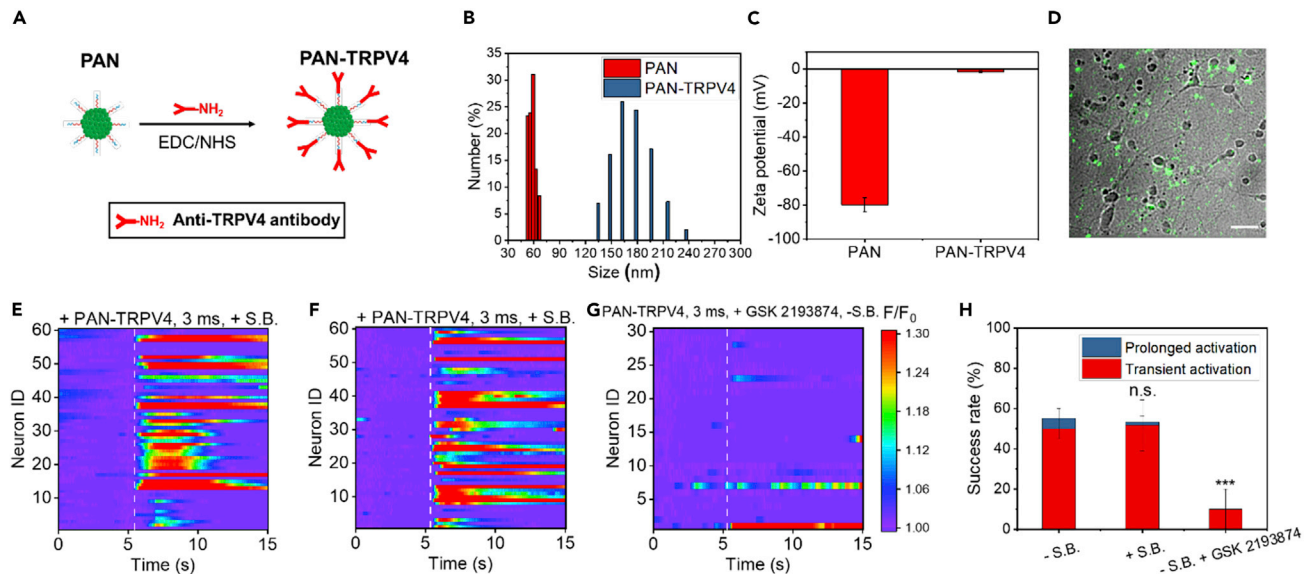


Figure 4. PAN-TRPV4 Induces Transient Activation of Neurons

(A) Schematic of PAN-TRPV4 synthesis.

(B) DLS analysis of PAN and PAN-TRPV4 sizes.

(C) Zeta-potential measurement of PAN and PAN-TRPV4 solutions.

(D) TA image of PAN-TRPV4 cultured with neurons for 15 min. Green, TA channel; gray, transmission channel. Scale bar, 50 μ m.

(E–G) Colormaps of fluorescence intensity change in neurons treated with PAN-TRPV4 without synaptic blockers (E), with the synaptic blocker cocktail (F), and with GSK 2193874 (G) added in the culture medium. A laser pulse train of 3 ms was used in all experiments.

(H) Success rate analysis. Error bars denote mean \pm SD. p value was calculated using without S.B. group as reference. n.s., not significant ($p > 0.5$); *** $p < 0.001$.

PANs Conjugated with TRPV4 Enable Channel-Specific Neural Stimulation

To enable specific targeting for stimulation, we bioconjugated the PANs with antibodies to specifically target the mechanosensitive ion channel transient receptor potential cation channel subfamily V member 4 (TRPV4). TRPV4 was chosen because of its high expression rate on the neuronal cell membranes and its capability of sensing external mechanical stimuli.^{51,52} We conjugated PANs with anti-TRPV4 antibody through a carbodiimide coupling reaction, using ethyl(dimethylaminopropyl) carbodiimide (EDC) and *N*-hydroxysuccinimide (NHS), between the carboxyl group on PANs and the amine group on the antibody (Figure 4A).²³ Successful bioconjugation was confirmed by comparing characteristics of PANs and anti-TRPV4 conjugated PANs (PAN-TRPV4). A size increase from 59.4 ± 5.3 nm to 181.8 ± 36.7 nm was revealed by DLS analysis (Figure 4B). The zeta potential for PAN-TRPV4 is -1.49 ± 0.38 mV, almost neutral and distinct from PANs (Figure 4C). No color change was noted in the PAN-TRPV4 solution (Figure S11A). No obvious shift in absorption spectrum was identified for the PAN-TRPV4 solution (Figure S11B).

We then confirmed the expression of the TRPV4 channels in the membrane of embryonic cortical neurons. As indicated on immunofluorescence staining images (Figure S12), TRPV4 channels are expressed vigorously throughout the soma and neurites of the neurons, as previously reported.^{53,54} This result indicates that a large number of target sites on the neuronal membrane are available for PAN-TRPV4 for potential binding. After incubation with PAN-TRPV4 for 15 min under the same conditions as for PANs, PAN-TRPV4 binding to neurons were visualized by TA microscopy (Figure 4D). The PAN-TRPV4 density was estimated to be 43.8 ± 20.8 per soma, slightly larger than that found for PAN binding.

Next, we studied whether PAN-TRPV4 could improve the specificity of neural stimulation through direct activation of TRPV4. Under the same experimental conditions used for PANs, we analyzed 60 neurons collected from five different culture batches. As shown in Figure 4E, neural activations induced by PAN-TRPV4 show an overall success rate of 55.0%, 50.0% \pm 5.0% of which is transient stimulation responses and 5.0% \pm 5.0% of which is the prolonged response (Figure S13). Although the overall success rate of PAN-TRPV4 was reduced slightly compared with PAN, the portion of transient activation increased substantially. As shown in Figure 4F, with the application of synaptic blocker cocktail, the overall success rate remains at 53.3%. 51.7% \pm 12.6% of neurons showed transient activation and only 1.7% \pm 2.9% showed prolonged activation, which indicates that PAN-TRPV4 induces more direct activation through targeting TRPV4 without significant involvement of neural network and synaptic transmission. To validate that the observed activation is mediated by the activation of the TRPV4 channel, we added the TRPV4 channel blocker, GSK 2193874,⁵⁵ into the culture, prior to adding PAN-TRPV4 solution (n = 30, collected from three different culture batches). As shown in Figure 4G, in the presence of GSK 2193874 the success rate significantly decreased, with 10.0% \pm 10.0% of the neurons showing transient response with no prolonged activation detected (Figure 4H). We further stimulated neurons with repeated photoacoustic stimulation using PAN-TRPV4. Four bursts of laser pulses, with a 3-ms duration in each burst and 10-s inter-burst interval, were delivered to the neurons cultured with PAN-TRPV4 for 15 min. Consistent calcium activations were observed (Figure S14). These results collectively show that PAN-TRPV4 enabled specific stimulation directly through the TRPV4 ion channel.

In Vivo Neural Stimulation by PANs

Upon successful stimulation of cultured primary neurons, we asked whether PANs could activate neurons *in vivo* in living animals. We directly injected 600 nL of 1.0 mg/mL PAN solution into the primary motor cortex of C57BL/6 mice using a stereotaxic injector at a controlled speed of 20 nL/min. Stimulation was performed 1 h after the injection. To validate brain activation, we performed local field potential (LFP) recording at the PAN injection site. To avoid electric artifact produced by laser radiation on the metal electrode, we used multifunctional fibers with a thick polymer coating as the recording electrodes (Figure S15).^{56,57} As shown in the Figures 5A and 5B, a 3-ms laser pulse train at 21 mJ/cm² produced a strong LFP response on the stimulated cortex, while in the control group on the contralateral side without PAN injection the laser irradiation did not produce any response.

With successful LFP recording of PAN stimulation in brain, we further evaluated the behavior outcome of the stimulation. We performed electromyography (EMG) as a measurement of the effect of PAN brain stimulation. PAN solution, 600 nL at 1.0 mg/mL, was injected into the primary motor cortex of the mouse. At 1 h after the injection, a needle electrode was inserted subcutaneously and parallel to the forelimb triceps brachii muscle. A reference electrode was inserted in the footpad with a ground electrode inserted subcutaneously on the trunk and ipsilateral to the stimulation site (Figure 5C). A 200-ms laser pulse train was delivered to the injection site through an optical fiber. EMG responses with an amplitude of 428.8 \pm 119.0 μ V and a delay of 127.8 \pm 24.3 ms were recorded (Figure 5D). These results suggest that PAN-mediated brain stimulation was sufficient to induce motor cortex activation and invoke subsequent motor responses.

PAN-Mediated Stimulation Is Not Thermally Induced

The photoacoustic effect is known to be associated with a temperature increase. To gain insights into how much the photothermal process might contribute to the

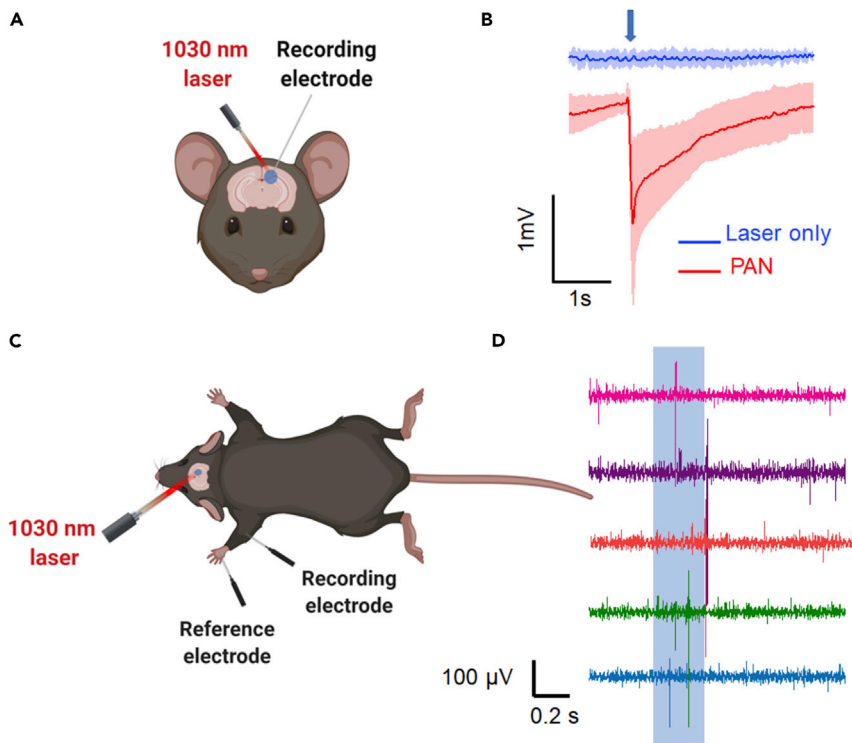


Figure 5. In Vivo Neural Stimulation by Injected PANs

(A) Schematic of *in vivo* electrophysiology measurement.

(B) Representative electrophysiology curves measured at the brain region without PANs as the control group (blue) and PAN-treated region (red) on three mice. Blue arrow indicates laser is on.

(C) Schematic of EMG recording.

(D) Forelimb EMG response to motor cortex PAN stimulation.

Data are presented as mean \pm SD.

successful activation discussed above, we performed neuron stimulation under continuous-wave (CW) laser. CW laser excitation of nanoparticles is known to produce a photothermal effect, resulting in a local temperature rise without generation of photoacoustic signals.⁵⁸ By comparing neural response to PANs upon excitation by the CW laser with that by the nanosecond laser at the same power, we can determine whether PAN-mediated stimulation differs from nanoparticle-mediated photothermal stimulation. Since PANs absorb broadly in the range of 800–1,300 nm, we used a CW laser at 1,064 nm. Identical neuronal culture conditions were used.

While we achieved successful neural activation under nanosecond laser power of 70 W/cm² and a train of 10 pulses over 3 ms, no activation was detected using CW laser excitation with the laser power of 70 W/cm² over 3.9-ms duration (n = 30, three different cell-culture batches, Figure 6A). No activation was observed as we increased the CW laser power to 397 W/cm² while maintaining the CW laser duration at 3.9 ms (n = 30, three different cell-culture batches, Figure 6B). Activation of neurons was only observed when the duration was increased to 2.5 s and laser power was increased to 397 W/cm² (n = 20, three different cell-culture batches, Figure S16). These results show that under the CW laser at comparable power and duration with nanosecond laser conditions, the photothermal effect produced by the PANs alone cannot result in neural activation. The photoacoustic function of PANs enabled by the nanosecond light pulse contributed dominantly to the activation.

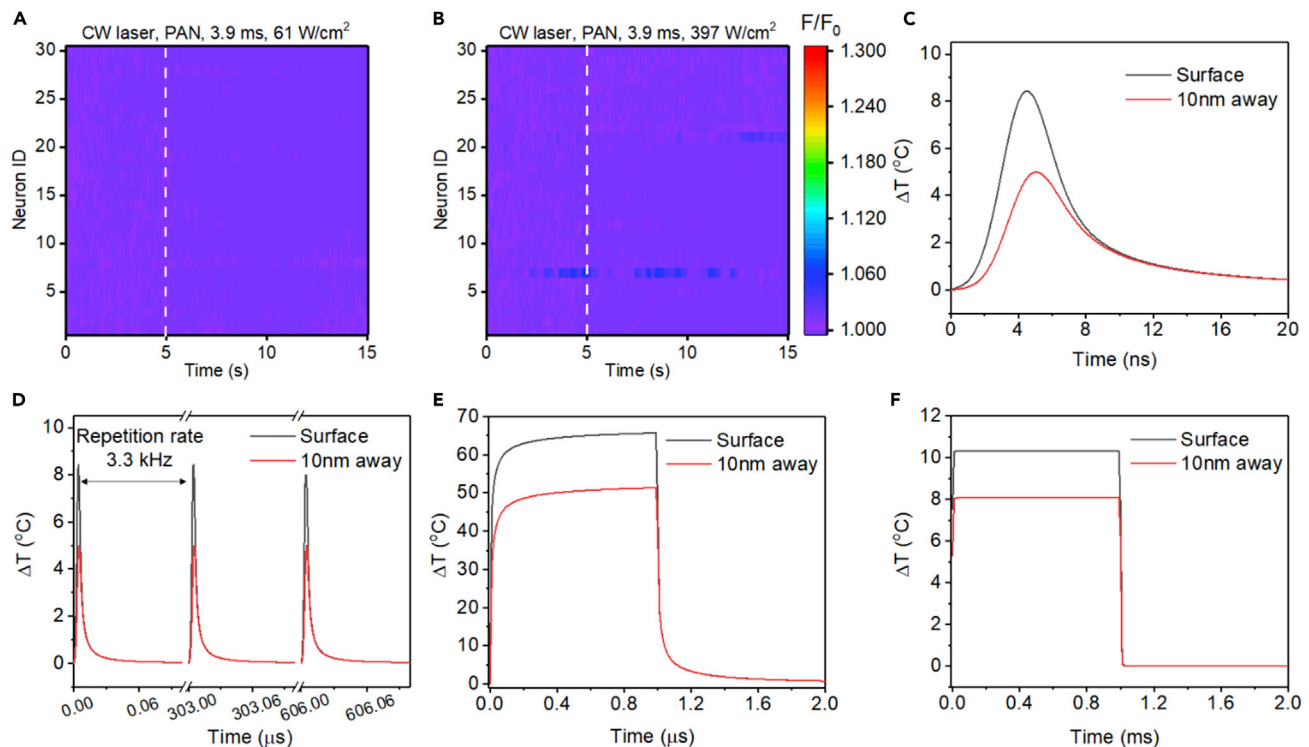


Figure 6. PAN-Mediated Neural Stimulation Is Not Thermally Induced

(A and B) Colormaps of fluorescence intensity change of neurons cultured with PANs under a 1,064-nm CW laser with laser condition of: (A) 3.9-ms laser duration and power density of 61 W/cm²; (B) 3.9-ms laser duration and power density of 397 W/cm². The colormaps were plotted under the same dynamic range. Neurons were cultured with PANs for 15 min before stimulation.

(C and D) COMSOL simulation on temperature changes with a single 3-ns laser pulse (C) and three 3-ns laser pulses with a 3.3-kHz repetition rate (D) on PAN surface (black) and 10 nm away from PAN surface in water (red). Laser wavelength is 1,030 nm. Pulse energy is 1.18 nJ.

(E and F) COMSOL simulation on temperature changes for a gold nanoparticle with 1-μs laser and pulse energy of 67.8 nJ (E), and gold nanoparticle with 1-ms laser with pulse energy of 9.8 μJ (F). Laser wavelength is 532 nm.

To understand how temperature rises and dissipates upon nanosecond laser excitation of a nanoparticle, we applied finite element modeling to simulate the evolution of PAN surface temperature in water. Simulation for temperature at 10 nm away from surface of PANs in water was also performed, aiming to probe the temperature of neuron membrane to which a PAN binds. Figure 6C shows how the PAN temperature evolves under excitation by a single 3-ns laser pulse at 1,030 nm. Pulse energy density of 2.1 mJ/cm² was used, consistent with the condition used in our PAN stimulation experiments. Temperature was found to quickly rise to a peak of 8.4°C on the PAN surface (black, Figure 6C) and to 5.0°C at 10 nm away from the PAN surface (red, Figure 6C). Importantly, in both cases the temperature decays to baseline within 10 ns from the peak value. We note that the laser pulse train used for PAN stimulation is operated with a repetition rate of 3.3 kHz. At this repetition rate, the laser pulse train resulted in pulsed temperature spikes with a full width at half maximum of 3 ns, and no temperature accumulation was observed (Figure 6D). For comparison, we simulated the temperature evolution for gold nanoparticles of 60-nm diameter under 532-nm CW laser with conditions reported for successful photothermal-driven optocapacitive stimulation. Two conditions, one with energy of 67.8 nJ and duration of 1 μs and the other with energy of 9.8 μJ and duration of 1 ms, were used with a laser focus of 5 μm diameter as previously described¹⁹ (Figures 6E and 6F). The temperature profile under these laser excitation conditions (Figures 6E and 6F) was found to be substantially different from the temperature profile

under nanosecond laser excitation (Figure S17). As shown in Figures 6E and 6F, the temperature increases on the gold nanoparticle surface quickly reach a plateau within the first 200 ns in both CW laser cases, with plateaued values at 65.6°C and 10.3°C, respectively. Similar temperature features were also found in our simulation of graphite microparticles under a laser energy of 0.7 μ J for 80 μ s laser duration at 532 nm, consistent with reported experimental and calculation results.^{20,21} In summary, in the case of PANs the maximum temperature increase is significantly smaller than in both CW cases. Additionally, the duration of each temperature spikes is a few nanoseconds, more than two orders smaller than that found for nanoparticle under CW laser excitation. It is conceivable that current induced by capacitance change over these tens of nanoseconds can be negligible. Together, our results suggest that PAN stimulation is distinct from photothermal optocapacitive stimulation.

DISCUSSION

In this work, we demonstrated semiconducting polymer-based PANs for neural stimulation under excitation by a nanosecond laser at the NIR-II. Enhanced specificity was achieved by bioconjugating TRPV4 to the PANs. Successful *in vivo* activation through PANs directly injected into the cortex area of mouse living brains was demonstrated by LFP and EMG recording.

The photothermal effect of nanoparticles has been reported to successfully modulate neurons mainly *in vitro*.^{15,17–19,23,59–63} Two potential stimulation mechanisms were proposed, one through the increase of temperature, with highest temperature often found in the range of 50°C–70°C,^{23,61} and another through an optocapacitive stimulation determined by the rate of temperature change.^{19–21} In our work, excited by a 3-ns pulsed laser, the maximum temperature rise on the PAN surface is 8°C and temperature change is in the form of 10 spikes, each of which is less than 10 ns in duration, without temperature accumulation over 3 ms. Instead, the PANs are able to generate a localized acoustic wave on the microsecond scale upon nanosecond pulsed light with a peak-to-peak pressure of 58.2 Pa at 10 nm from the PAN surface (Figure S17). Activation did not occur when we changed the nanosecond laser to a CW laser of the same energy (Figures 6A and 6B). We note that in addition to its mechanosensitivity, TRPV4 is also sensitive to mild temperature increases, specifically when temperature exceeds 32°C for neurons initially under room temperature.⁶⁴ Based on our simulation, the surface temperature increase of 8°C (from 20°C to 28°C) under nanosecond light excitation is not sufficient to evoke TRPV4 current by heat alone. These findings collectively show that PAN neural stimulation observed is mainly contributed by the photoacoustic effect. Nevertheless, whenever such experiments are performed under body temperature, the possibility of heat-induced activation should be further investigated.

Since PANs generate acoustic waves with ultrasonic frequencies, it is likely that PAN-mediated stimulation shares the mechanisms of ultrasound neuromodulation. Several possible mechanisms have been proposed for ultrasound neuromodulation,^{65,66} and activation of mechanosensitive ion channels is among the most studied in the literature.^{67–69} In this work, we showed that direct binding to TRPV4 enhances stimulation specificity and efficiency, which suggests activation of mechanosensitive channels as a potential mechanism candidate for future investigations. Nevertheless, other mechanosensitive channels including TRPC4, Piezo1, TREK-1, and TRAAK channels^{70–75} should also be considered and further investigated. Other possible mechanisms involve transient mechanical disruptions of the neuronal membrane, which includes permeability change induced by membrane sonoporation^{76,77} and capacitive current generated by intramembrane cavitation.^{78,79}

Notably, when thermal confinement was met, many nanoparticles, including gold nanoparticles, can also be photoacoustic.⁸⁰ The photoacoustic properties of these nanostructures have been only applied for photoacoustic imaging. Our work is the first demonstration of photoacoustic nanoparticles for neurostimulation. The semiconducting polymer-based PAN provides a new paradigm for neural modulation through offering three important features compared with other photoacoustic agents. First, we compared COMSOL simulation for gold nanoparticles under nanosecond laser conditions at the wavelength of 532 nm (Figure S18) with that for PANs. Under the same laser power, the maximum temperature rise is 40.4°C on the gold nanoparticle surface, compared with 8.4°C on the PAN surface. As it produces less temperature rise, avoiding potential thermal toxicity while effectively activating neurons, the PAN is of particular interest for neuron stimulation. Second, semiconducting polymer nanoparticles have been shown to have biocompatibility and biodegradability. Our results also confirmed that PANs induce minimal cytotoxicity to neurons *in vitro*. Additionally, through an engineered metabolizing pathway, biodegradation of semiconducting polymer nanoparticles has been recently demonstrated *in vitro* and *in vivo*,^{24,81} which potentially allows clearance of PANs from the brain after stimulation. Third, PANs provide an exciting opportunity for non-invasive neural modulation and other biological regulation.⁸² PANs uniquely absorb NIR-II light. Due to its longer wavelength, NIR-II light has been reported to have sufficient penetration depth in highly scattering medium.^{30,83,84} Such wavelength has also been demonstrated to have the capability of penetrating the human skull,^{27,28} potentially enabling non-surgical brain stimulation through light excitation. To illustrate the possibility for deep penetration, we embedded PANs in a 5-mm-thick brain-mimicking phantom under a mouse skull. We clearly detected photoacoustic signals from these PANs by nanosecond laser excitation above the skull using photoacoustic tomography (Figure S19). In addition, advances in biophotonics showed that NIR light focusing with approximately 100 μm is possible in brain tissue.⁸⁵ Compared with other studies on NIR-absorbing upconversion nanoparticle-assisted optogenetic neural modulation,^{86–89} PAN neural modulation does not require genetic modification, which makes it suitable for potential clinical applications in human subjects. Additionally, compared with photothermal neuromodulation based on light-absorbing nanoparticles,^{23,61,88,90} often with CW laser, PAN-mediated stimulation shows no thermal accumulation, which largely eliminates thermally induced tissue damage. Together with potential development in surgical free targeted delivery of PANs to specific regions of brain, for example, via ultrasound opening of the blood-brain barrier,^{91,92} PANs promise the opportunity of non-genetic and non-surgical brain modulation in live animals and eventually in human patients.

EXPERIMENTAL PROCEDURES

Resource Availability

Lead Contact

Further information and requests for resources and reagents should be directed to and will be fulfilled by the Lead Contact, Chen Yang (cheyang@bu.edu).

Materials Availability

The synthesized polymer may be requested from the authors.

Data and Code Availability

All data needed to evaluate the conclusions in the paper are present in the paper and/or [Supplemental Information](#). Additional data related to this paper may be requested from the authors. Codes used for COMSOL may be requested from the authors.

Materials

All chemical reagents were purchased from Sigma-Aldrich (MO, USA) unless otherwise stated. The semiconducting polymer was synthesized via palladium-catalyzed C–C cross-coupling techniques and was thoroughly purified to remove any metal residues. The TRPV4 antibody powders were purchased from the Aloemone laboratory and used without further modification.

Synthesis of PAN

Following the previously developed synthesis process,³⁰ the polymers were dissolved in THF (1 mg/mL) with surfactant PS-PAA (5 mg/mL) rapidly injected into deionized water (9 mL) under continuous sonication with a microtip-equipped probe sonicator (Branson, W-150) at a power output of 6 W for 30 s. After sonication for an additional 1 min, THF was removed by nitrogen bubbling for 3 h. The aqueous solution was filtered through a polyethersulfone (PES) syringe-driven filter (0.22 μ m) and centrifuged three times using a 30K centrifugal filter unit at 3,500 rpm for 15 min. PAN solution was stored in darkness at 4°C for further use.

Characterization

DLS and zeta-potential measurements were performed on a Brookhaven 90plus nanoparticle sizer with zeta potential. UV-visible-NIR spectra were recorded on a Cary 5000 spectrophotometer. FTIR spectrum was taken on a Bruker Optics Vertex 70v FTIR instrument equipped with a Hyperion microscope and Silicon Bolometer. Low-resolution TEM was taken using a Philips CM12 operated at 100 kV. Images were recorded on a TVIPS CMOS F216 camera.

Photoacoustic Measurement of PANs

The PAN solution (1 mg/mL) was added into a polyurethane capillary tube with two ends fixed with epoxy. A customized and compact passively Q-switched diode-pumped solid-state laser (1,030 nm, 3 ns, 100 μ J, repetition rate 3.3 kHz; RPMC, Fallon, MO, USA) was used as the excitation source. The laser was connected to an optical fiber through a homemade fiber jumper (SMA-to-SC/PC, ~81% coupling efficiency). The laser was adjusted to set the output power from the fiber jumper to be approximately 55 mW. The capillary tube was fixed in the water tank. One miniaturized ultrasound transducer with a central frequency of 5 MHz (XMS-310-B; Olympus, Waltham, MA, USA) was used to record the photoacoustic signals. The ultrasonic signal was first amplified by an ultrasonic preamplifier (0.2–40 MHz, 40 dB gain, Model 5678; Olympus) and then sent to an oscilloscope (DSO6014A; Agilent Technologies, Santa Clara, CA, USA) for readout. The signal was averaged 20 times. The pressure of the photoacoustic waves generated was calibrated using a hydrophone with a diameter of 2 mm and frequency range of 1–20 MHz (Precision Acoustics, Dorchester, UK). All of the devices were synchronized by the output from the active monitoring photodiode inside the laser.

Animals

Embryonic day 15–18 (E15–E18) rats, obtained from pregnant Sprague-Dawley rats, were used for preparing cell culture used in the *in vitro* experiments. Adult (age 14–16 weeks) C57BL/6J mice were used for *in vivo* experiments. All animal care was carried out in accordance with the National Institutes of Health Guide for the Care and Use of Laboratory Animals (NIH Publications No. 80-23; revised 1996) and was operated under protocol 17-022 approved by Boston University Animal Care and Use Committee.

Embryonic Neuron Culture

The glass-bottomed culture dishes used in the embryonic neuron cell cultures were immersed in 0.01% poly-D-lysine (Sigma-Aldrich, MO) overnight at 4°C and washed in PBS before culture initiation. Primary cortical neurons were obtained from Sprague-Dawley rats. Cortices were dissected out from E15–E18 rats of either sex and digested in 0.05% trypsin/EDTA (VWR, PA, USA) for 15 min at 37°C and triturated every 5 min. Dissociated cells were washed with and triturated in 10% heat-inactivated fetal bovine serum (FBS; Atlanta Biologicals, GA, USA), 5% heat-inactivated horse serum (HS; Atlanta Biologicals), 2 mM glutamine-Dulbecco's modified Eagle's medium (DMEM; Thermo Fisher Scientific, MA, USA), and cultured in cell-culture dishes (100 mm diameter) for 30 min at 37°C to eliminate glial cells and fibroblasts. The supernatant containing neurons was collected and seeded on a poly-D-lysine-coated coverglass and incubated in a humidified atmosphere containing 5% CO₂ at 37°C with 10% FBS + 5% HS + 2 mM glutamine-DMEM. After 16 h, the medium was replaced with Neurobasal medium containing 2% B27, 1% N2, and 2 mM glutamine (all from Thermo Fisher Scientific).

TA Microscopy

TA images were obtained as previously described.^{41,42,93} For each TA image, the Z position of the focus was adjusted near the equatorial plane of the neurons so that the soma and neurites were both clearly visualized. The pump (1,045 nm) and probe (845 nm) powers before the microscope were maintained at 20 mW and 20 mW, respectively. Both the pump and probe beams were linearly polarized. No cell or tissue damage was observed. Images were acquired at pixel dwell time of 2 μs.

To quantify the number of PANs that bind onto neurons, we used the following estimation. An effective concentration of bound PANs can be estimated based on the TA intensity in the image and the TA calibration curve. The TA calibration curve was obtained from TA images acquired for PAN solutions with known concentrations. The volume occupied by the bound PANs or PAN-TRPV4 was estimated based on the area of bounded PANs on neuronal soma (measured from ImageJ) and TA focal depth of 1 μm. The molecular weights of PAN and PAN-TRPV4 were estimated based on electrophoresis measurement to be 75 kDa and 125 kDa. The number of PANs or PAN-TRPV4 was calculated based on the aforementioned parameters.

Cytotoxicity Tests

Neurons were seeded in 96-well plates (1,000 cells/well in 100 μL) and incubated. PAN solution with concentrations of 20, 40, and 60 μg/mL was added to the cell-culture medium, respectively. Neurons were incubated with PANs or cell-culture medium only for 1 h and 24 h, respectively. The medium was then removed and washed with PBS. MTT (20 μL, 5 mg/mL) was added to the wells and incubated for 5 h. The cell-culture medium was then removed, and 200 μL of dimethylsulfoxide (DMSO) was subsequently added to each well. Finally, the plates were gently shaken for 10 min at room temperature to dissolve all formed precipitates. The absorbance of MTT at 590 nm was measured using a SpectraMax plate reader. Cell viability was expressed as the ratio of the absorbance of the cells incubated with PANs to that of control.

Cell viability under stimulation conditions was also tested. Neurons at DIV 15 were cultured with PANs for 15 min. During stimulation, laser pulse trains of 3 ms at 3.3 kHz were applied to neurons at 27, 35, and 57 μJ pulse energy, respectively using the same fiber-delivery method as described below. Two stimulation protocols were applied: one 3-ms pulse train (one stimulation) and three 3-ms pulse trains

with intervals of 30 s (three stimulations). Two control groups were also tested, a light-only group of neurons going through the same laser application as the stimulation protocol without PANs added and another group of neurons with no PANs or laser illumination (CTR). One hour after stimulation or light application, neurons were labeled with SYTOX Green (Thermo Fisher) at 10 $\mu\text{M}/\text{mL}$ for 30 min, and fluorescence imaging was performed. Cell viabilities were calculated by: (number of SYTOX-negative neurons)/(total number of neurons). All experiments were repeated three times.

Synthesis of PAN-TRPV4

PAN solution (1 mL, 20 $\mu\text{g}/\text{mL}$) was combined with 10 \times PBS (110 μL , pH 7.4), followed by NHS (30 μL , 9 mg/mL) and EDC (50 μL , 9 mg/mL). The mixture was stirred for 1 h at room temperature in darkness. Anti-TRPV4 antibody (5 μL , 1 mg/mL) was added into the mixture and stirred at room temperature overnight. The resulting solution was filtered through a PES syringe-driven filter (0.22 μm) and centrifuged three times using a 50K centrifugal filter unit at 3,500 rpm for 15 min. PAN-TRPV4 solution was stored in darkness at 4°C for further use.

Immunofluorescence Imaging

Cells were fixed with 4% paraformaldehyde for 20 min. After three washes, cells were blocked in 5% BSA (Sigma-Aldrich, MO, USA) for 30 min and permeabilized with 0.2% Triton X-100 (Sigma-Aldrich). Cells were then incubated with mouse monoclonal anti-TRPV4 (1:1,000) antibody for 2 h, then with goat anti-mouse secondary antibody (1:1,000, 488 nm; Thermo Fisher Scientific) for 1 h at room temperature. The fluorescence images were taken with a home-built wide-field fluorescence microscope (Olympus).

In Vitro Neurostimulation

PAN or PAN-TRPV4 (150 μL , 20 $\mu\text{g}/\text{mL}$) solution was added into the culture medium of GCaMP6f-labeled neurons to reach a final concentration of 2 $\mu\text{g}/\text{mL}$. An incubation time of 15 min and 1 h was tested. A Q-switched 1,030-nm nanosecond laser (Bright Solution) was used. For the CW laser, a Cobolt Rumba 1,064-nm 500-mW laser was used. The CW laser was gated with a mechanical shutter to control the laser duration. The laser was delivered using an optical fiber (Thorlabs) with a diameter of 200 μm and 0.22 NA. During neurostimulation experiments, the fiber was placed approximately 100 μm above the neurons and the illumination area was calculated to be 222.27 μm . Calcium fluorescence imaging was performed on a lab-built wide-field fluorescence microscope. The microscope was based on an Olympus IX71 microscope frame with a 20 \times air objective (UPLSAPO20 \times , 0.75 NA; Olympus) illuminated by a 470-nm LED (M470L2; Thorlabs), and a dichroic mirror (DMLP505R; Thorlabs). Image sequences were acquired with a scientific CMOS camera (Zyla 5.5; Andor) at 20 frames per second. The fluorescence intensity analysis and exponential curve fitting were performed using ImageJ (Fiji).

In Vivo Injection of PANs

Adult (age 14–16 weeks) C57BL/6J mice were used. Mice were initially anesthetized using 5% isoflurane in oxygen and then placed on a standard stereotaxic frame, maintained with 1.5%–2% isoflurane. Toe pinch was used to determine the level of anesthesia throughout the experiments, and body temperature was maintained with a heating pad. The hair and skin on the dorsal surface targeted brain regions were trimmed. Craniotomies were made on primary motor cortex based on stereotaxic coordinates using a dental drill, and artificial cortical spinal fluid was administered to immerse the brain. PAN solution with a concentration of 1.0 mg/mL was

injected into the primary motor cortex using a quintessential stereotaxic injector (Stoelting) with a speed of 20 nL/min for 30 min. The injected PANs were allowed to diffuse for 1 h before stimulation experiments. Optical fiber with a diameter of 200 μm was coupled to a micromanipulator to control the illumination position.

In Vivo LFP Recording

Electrophysiology was performed using multifunctional fibers with a thick polymer coating as the recording electrodes.^{56,57} The electrodes were positioned with a micromanipulator to the targeted brain region (Siskiyou). Extracellular recordings were acquired using a Multi-Clamp 700B amplifier (Molecular Devices), filtered at 0.1 to 100 Hz, and digitized with an Axon DigiData 1550 digitizer (Molecular Devices).

EMG Recording

EMG was performed using a needle electrode inserted subcutaneously and parallel to the forelimb triceps brachii muscle. Reference electrode was inserted in the footpad. A ground electrode was inserted subcutaneously on the trunk and ipsilateral to the stimulation site. EMG signals were acquired using a Multi-Clamp 700B amplifier (Molecular Devices), filtered at 1 to 5000 Hz, and digitized with an Axon DigiData 1,550 digitizer (Molecular Devices).

COMSOL Simulation

The temperature change on PANs and gold nanoparticles was simulated in COMSOL Multiphysics (COMSOL, USA). The size of the nanoparticles for both PANs and gold nanoparticles was set to be 60 nm. The laser irradiation on a single PAN was assumed to be uniform. The surrounding environment was water. The absorption cross-sections of both PANs and gold nanoparticles were calculated according to Mie scattering theory.⁹⁴ To calculate the temperature change induced by laser irradiation, we used the heat transfer module. The simulation model was validated first by comparing the simulation results with the experimental data reported previously.¹⁸

Photoacoustic Tomography

The photoacoustic signals were processed by a high-frequency ultrasound imaging system (Vantage 128; Verasonics). A brain-mimicking phantom (10% gelatin, 1% formaldehyde, and 5% intralipid) was used to mimic the highly scattered brain tissue.⁹⁵ A piece of mouse skull was placed on top of the phantom to test the penetration depth of NIR-II light. PAN solution with a concentration of 1.5 mg/mL in a transparent polyurethane tube was placed under the phantom. A Q-switched Nd:YAG laser (CFR ICE450; Quantel Laser) with 8-ns pulse width and 10-Hz repetition rate was applied as the excitation. The wavelength was set to be 1,100 nm and laser power was fixed to be 9 mJ. The laser light was guided to the surface of the mouse skull by a fiber bundle, and the photoacoustic signals were detected from the other side of the tissue by a low-frequency transducer array (L7-4; Philips/ATL).

Data Analysis

Calcium images were analyzed using ImageJ. Calcium traces, electrophysiological traces, and EMG recordings were analyzed and plotted using Origin and MATLAB. All statistical analyses were done using Origin. Data shown are mean \pm standard deviation (SD). *p* values were calculated based on two-sample *t* test and defined as: n.s., not significant ($p > 0.5$); * $p < 0.5$; ** $p < 0.01$; *** $p < 0.001$.

SUPPLEMENTAL INFORMATION

Supplemental Information can be found online at <https://doi.org/10.1016/j.matt.2020.11.019>.

ACKNOWLEDGMENTS

This work was supported by Boston University Nanotechnology Innovation Center Cross-Disciplinary fellowship for Y.H.; National Institutes of Health, United States, R01 NS109794 to J.-X.C. and C.Y.; National Science Foundation, United States, 1653909; National Science Foundation, United States 1847436 to X.J.; and National Science Foundation, United States, CAREER 1653909 to J.M. We thank Margaret O'Connor, Zachary Gardner, and Yuan Tian for their assistance in the preparation of primary neuronal cultures.

AUTHOR CONTRIBUTIONS

C.Y. and J.-X.C. conceived the concept of using PANs for neuromodulation; X.L. and J.M. synthesized the semiconducting polymer; Y.H., J.W., and R.C. synthesized PAN; Y.H. and Y.J. designed and performed the experiments; Y.H., Y.J., S.L., L.L., H.-Y.M., J.-X.C., and C.Y. discussed and analyzed the data; H.-Y.M. provided neuron cultures; S.J. and X.J. designed and fabricated the multifunction electrode for *in vivo* LFP recording; H.Z. performed the COMSOL simulation; Y.H., Y.J., and C.Y. wrote the manuscript. All authors discussed and edited the manuscript. C.Y. and J.C. supervised the project.

DECLARATION OF INTERESTS

The authors declare no competing interests.

Received: September 7, 2020

Revised: October 27, 2020

Accepted: November 25, 2020

Published: December 22, 2020

REFERENCES

- Perlmutter, J.S., and Mink, J.W. (2006). Deep brain stimulation. *Annu. Rev. Neurosci.* *29*, 229–257.
- Hallett, M. (2000). Transcranial magnetic stimulation and the human brain. *Nature* *406*, 147–150.
- Brunoni, A.R., Nitsche, M.A., Bolognini, N., Bikson, M., Wagner, T., Merabet, L., Edwards, D.J., Valero-Cabre, A., Rotenberg, A., Pascual-Leone, A., et al. (2012). Clinical research with transcranial direct current stimulation (tDCS): challenges and future directions. *Brain Stimul.* *5*, 175–195.
- Zhang, F., Gradinaru, V., Adamantidis, A.R., Durand, R., Airan, R.D., de Lecea, L., and Deisseroth, K. (2010). Optogenetic interrogation of neural circuits: technology for probing mammalian brain structures. *Nat. Protoc.* *5*, 439–456.
- Yizhar, O., Fenno, L.E., Davidson, T.J., Mogri, M., and Deisseroth, K. (2011). Optogenetics in neural systems. *Neuron* *71*, 9–34.
- Gilbert, F., Harris, A.R., and Kapsa, R.M.I. (2014). Controlling brain cells with light: ethical considerations for optogenetic clinical trials. *AJOB Neurosci.* *5*, 3–11.
- Tufail, Y., Matyushov, A., Baldwin, N., Tauchmann, M.L., Georges, J., Yoshihiro, A., Tillery, S.I.H., and Tyler, W.J. (2010). Transcranial pulsed ultrasound stimulates intact brain circuits. *Neuron* *66*, 681–694.
- Tufail, Y., Yoshihiro, A., Pati, S., Li, M.M., and Tyler, W.J. (2011). Ultrasonic neuromodulation by brain stimulation with transcranial ultrasound. *Nat. Protoc.* *6*, 1453–1470.
- Deffieux, T., Younan, Y., Wattiez, N., Tanter, M., Pouget, P., and Aubry, J.-F. (2013). Low-intensity focused ultrasound modulates monkey visuomotor behavior. *Curr. Biol.* *23*, 2430–2433.
- Legon, W., Sato, T.F., Opitz, A., Mueller, J., Barbour, A., Williams, A., and Tyler, W.J. (2014). Transcranial focused ultrasound modulates the activity of primary somatosensory cortex in humans. *Nat. Neurosci.* *17*, 322.
- Legon, W., Bansal, P., Tyshynsky, R., Ai, L., and Mueller, J.K. (2018). Transcranial focused ultrasound neuromodulation of the human primary motor cortex. *Sci.Rep.* *8*, 10007.
- Legon, W., Rowlands, A., Opitz, A., Sato, T.F., and Tyler, W.J. (2012). Pulsed ultrasound differentially stimulates somatosensory circuits in humans as indicated by EEG and fMRI. *PLoS One* *7*, e51177.
- Mueller, J., Legon, W., Opitz, A., Sato, T.F., and Tyler, W.J. (2014). Transcranial focused ultrasound modulates intrinsic and evoked EEG dynamics. *Brain Stimul.* *7*, 900–908.
- Jiang, Y., Lee, H.J., Lan, L., Tseng, H.-a., Yang, C., Man, H.-Y., Han, X., and Cheng, J.-X. (2020). Optoacoustic brain stimulation at submillimeter spatial precision. *Nat. Commun.* *11*, <https://doi.org/10.1038/s41467-020-14706-1>.
- Carvalho-de-Souza, J.L., Treger, J.S., Dang, B., Kent, S.B., Pepperberg, D.R., and Bezanilla, F. (2015). Photosensitivity of neurons enabled by cell-targeted gold nanoparticles. *Neuron* *86*, 207–217.
- Yong, J., Needham, K., Brown, W.G.A., Nayagam, B.A., McArthur, S.L., Yu, A., and Stoddart, P.R. (2014). Gold-nanorod-assisted near-infrared stimulation of primary auditory neurons. *Adv. Healthc. Mater.* *3*, 1862–1868.

17. Eom, K., Im, C., Hwang, S., Eom, S., Kim, T.S., Jeong, H.S., Kim, K.H., Byun, K.M., Jun, S.B., and Kim, S.J. (2016). Synergistic combination of near-infrared irradiation and targeted gold nanoheaters for enhanced photothermal neural stimulation. *Biomed. Opt. Express* **7**, 1614–1625.
18. Carvalho-de-Souza, J.L., Nag, O.K., Oh, E., Huston, A.L., Vurgaftman, I., Pepperberg, D.R., Bezanilla, F., and Delehanty, J.B. (2019). Cholesterol functionalization of gold nanoparticles enhances photoactivation of neural activity. *ACS Chem. Neurosci.* **10**, 1478–1487.
19. Carvalho-de-Souza, J.L., Pinto, B.I., Pepperberg, D.R., and Bezanilla, F. (2018). Optocapacitive generation of action potentials by microsecond laser pulses of nanojoule energy. *Biophys. J.* **114**, 283–288.
20. Farah, N., Zoubi, A., Matar, S., Golan, L., Marom, A., Butson, C.R., Brosh, I., and Shoham, S. (2013). Holographically patterned activation using photo-absorber induced neural-thermal stimulation. *J. Neural Eng.* **10**, <https://doi.org/10.1088/1741-2560/10/5/056004>.
21. Weissler, Y., Farah, N., and Shoham, S. (2017). Simulation of morphologically structured photo-thermal neural stimulation. *J. Neural Eng.* **14**, <https://doi.org/10.1088/1741-2552/aa7805>.
22. Parameswaran, R., Carvalho-de-Souza, J.L., Jiang, Y.W., Burke, M.J., Zimmerman, J.F., Koehler, K., Phillips, A.W., Yi, J., Adams, E.J., Bezanilla, F., et al. (2018). Photoelectrochemical modulation of neuronal activity with free-standing coaxial silicon nanowires. *Nat. Nanotechnol.* **13**, 260–266.
23. Lyu, Y., Xie, C., Chechetka, S.A., Miyako, E., and Pu, K. (2016). Semiconducting polymer nanobioconjugates for targeted photothermal activation of neurons. *J. Am. Chem. Soc.* **138**, 9049–9052.
24. Jiang, Y., Upputuri, P.K., Xie, C., Zeng, Z., Sharma, A., Zhen, X., Li, J., Huang, J., Pramanik, M., and Pu, K. (2019). Metabolizable semiconducting polymer nanoparticles for second near-infrared photoacoustic imaging. *Adv. Mater.* **31**, 1808166.
25. Chen, R., Romero, G., Christiansen, M.G., Mohr, A., and Anikeeva, P. (2015). Wireless magnetothermal deep brain stimulation. *Science* **347**, 1477–1480.
26. Yue, K., Guduru, R., Hong, J.M., Liang, P., Nair, M., and Khizroev, S. (2012). Magneto-electric nano-particles for non-invasive brain stimulation. *PLoS One* **7**, <https://doi.org/10.1371/journal.pone.0044040>.
27. Henderson, T.A., and Morries, L.D. (2015). Near-infrared photonic energy penetration: can infrared phototherapy effectively reach the human brain? *Neuropsychiatr. Dis. Treat.* **11**, 2191–2208.
28. Hamblin, M.R. (2016). Shining light on the head: photobiomodulation for brain disorders. *BBA Clin.* **6**, 113–124.
29. Luo, X., Tran, D.T., Sun, H., Mi, T., Kadlubowski, N.M., Zhao, Y., Zhao, K., and Mei, J. (2018). Bis-iodindigos: new electron-deficient building blocks for constructing conjugated polymers with extended electron delocalization. *Asian J. Org. Chem.* **7**, 2248–2253.
30. Wu, J.Y.Z., You, L.Y., Lan, L., Lee, H.J., Chaudhry, S.T., Li, R., Cheng, J.X., and Mei, J.G. (2017). Semiconducting polymer nanoparticles for centimeters-deep photoacoustic imaging in the second near-infrared window. *Adv. Mater.* **29**, <https://doi.org/10.1002/adma.201703403>.
31. Wang, L.V. (2017). *Photoacoustic Imaging and Spectroscopy* (CRC Press).
32. Dante, S., Petrelli, A., Petrini, E.M., Marotta, R., Maccione, A., Alabastri, A., Quarta, A., De Donato, F., Ravasenga, T., Sathya, A., et al. (2017). Selective targeting of neurons with inorganic nanoparticles: revealing the crucial role of nanoparticle surface charge. *ACS Nano* **11**, 6630–6640.
33. Zhu, Y., and Cheng, J.-X. (2020). Transient absorption microscopy: technological innovations and applications in materials science and life science. *J. Chem. Phys.* **152**, 020901.
34. Zhu, T., Snaider, J.M., Yuan, L., and Huang, L. (2019). Ultrafast dynamic microscopy of carrier and exciton transport. *Annu. Rev. Phys. Chem.* **70**, 219–244.
35. Fischer, M.C., Wilson, J.W., Robles, F.E., and Warren, W.S. (2016). Invited review article: pump-probe microscopy. *Rev. Sci. Instr.* **87**, 031101.
36. Beane, G., Devkota, T., Brown, B.S., and Hartland, G.V. (2018). Ultrafast measurements of the dynamics of single nanostructures: a review. *Rep. Prog. Phys.* **82**, 016401.
37. Chen, A.J., Yuan, X., Li, J., Dong, P., Hamza, I., and Cheng, J.-X. (2018). Label-free imaging of heme dynamics in living organisms by transient absorption microscopy. *Anal. Chem.* **90**, 3395–3401.
38. Dong, P.-T., Lin, H., Huang, K.-C., and Cheng, J.-X. (2019). Label-free quantitation of glycated hemoglobin in single red blood cells by transient absorption microscopy and phasor analysis. *Sci. Adv.* **5**, eaav0561.
39. Fu, D., Ye, T., Matthews, T.E., Grichnik, J.M., Hong, L., Simon, J.D., and Warren, W.S. (2008). Probing skin pigmentation changes with transient absorption imaging of eumelanin and pheomelanin. *J. Biomed. Opt.* **13**, 054036.
40. Matthews, T.E., Piletic, I.R., Selim, M.A., Simpson, M.J., and Warren, W.S. (2011). Pump-probe imaging differentiates melanoma from melanocytic nevi. *Sci. Transl. Med.* **3**, 71ra15.
41. Jung, Y., Slipchenko, M.N., Liu, C.H., Ribbe, A.E., Zhong, Z., Yang, C., and Cheng, J.X. (2010). Fast detection of the metallic state of individual single-walled carbon nanotubes using a transient-absorption optical microscope. *Phys. Rev. Lett.* **105**, 217401.
42. Tong, L., Liu, Y., Dolash, B.D., Jung, Y., Slipchenko, M.N., Bergstrom, D.E., and Cheng, J.X. (2011). Label-free imaging of semiconducting and metallic carbon nanotubes in cells and mice using transient absorption microscopy. *Nat. Nanotechnol.* **7**, 56–61.
43. Huang, K.-C., McCall, J., Wang, P., Liao, C.-S., Eakins, G., Cheng, J.-X., and Yang, C. (2018). High-speed spectroscopic transient absorption imaging of defects in graphene. *Nano Lett.* **18**, 1489–1497.
44. Guo, Z., Wan, Y., Yang, M., Snaider, J., Zhu, K., and Huang, L. (2017). Long-range hot-carrier transport in hybrid perovskites visualized by ultrafast microscopy. *Science* **356**, 59–62.
45. Huang, L., Hartland, G.V., Chu, L.-Q., Feenstra, R.M., Lian, C., Tahy, K., and Xing, H. (2010). Ultrafast transient absorption microscopy studies of carrier dynamics in epitaxial graphene. *Nano Lett.* **10**, 1308–1313.
46. Lo, S.S., Shi, H.Y., Huang, L., and Hartland, G.V. (2013). Imaging the extent of plasmon excitation in Au nanowires using pump-probe microscopy. *Opt. Lett.* **38**, 1265–1267.
47. Wu, J., Lee, H.J., You, L., Luo, X., Hasegawa, T., Huang, K.C., Lin, P., Ratliff, T., Ashizawa, M., and Mei, J. (2020). Functionalized NIR-II semiconducting polymer nanoparticles for single-cell to whole-organ imaging of PSMA-positive prostate cancer. *Small* **16**, 2001215.
48. Wu, J., Zhu, Y., You, L., Dong, P.T., Mei, J., and Cheng, J.X.J.A.F.M. (2020). Polymer electrochromism driven by metabolic activity facilitates rapid and facile bacterial detection and susceptibility evaluation. *Adv. Funct. Mater.* **293**, 2005192.
49. Jones, L.J., and Singer, V.L. (2001). Fluorescence microplate-based assay for tumor necrosis factor activity using SYTOX Green stain. *Anal. Biochem.* **293**, 8–15.
50. Chang, M.C., Park, J.M., Pelkey, K.A., Grabenstatter, H.L., Xu, D.S., Linden, D.J., Sutula, T.P., McBain, C.J., and Worley, P.F. (2010). Narp regulates homeostatic scaling of excitatory synapses on parvalbumin-expressing interneurons. *Nat. Neurosci.* **13**, 1090–U1083.
51. Kanju, P., and Liedtke, W. (2016). Pleiotropic function of TRPV4 ion channels in the central nervous system. *Exp. Physiol.* **101**, 1472–1476.
52. Plant, T.D., and Strotmann, R. (2007). TRPV4: a multifunctional nonselective cation channel with complex regulation. In *TRP Ion Channel Function in Sensory Transduction and Cellular Signaling Cascades*, W.B. Liedtke and S. Heller, eds. (CRC Press), pp. 125–140.
53. Uhlen, M., Fagerberg, L., Hallstrom, B.M., Lindskog, C., Oksvold, P., Mardinoglu, A., Sivertsson, A., Kampf, C., Sjostedt, E., Asplund, A., et al. (2015). Tissue-based map of the human proteome. *Science* **347**, <https://doi.org/10.1126/science.1260419>.
54. Uhlen, M., Oksvold, P., Fagerberg, L., Lundberg, E., Jonasson, K., Forsberg, M., Zwahlen, M., Kampf, C., Wester, K., Hober, S., et al. (2010). Towards a knowledge-based human protein atlas. *Nat. Biotechnol.* **28**, 1248–1250.
55. Thorneloe, K.S., Cheung, M., Bao, W., Alsaïd, H., Lenhard, S., Jian, M.Y., Costell, M., Maniscalco-Hauk, K., Krawiec, J.A., Olzinski, A., et al. (2012). An orally active TRPV4 channel blocker prevents and resolves pulmonary edema induced by heart failure. *Sci. Transl. Med.* **4**, 159ra148.

56. Canales, A., Jia, X.T., Frierie, U.P., Koppes, R.A., Tringides, C.M., Selvidge, J., Lu, C., Hou, C., Wei, L., Fink, Y., et al. (2015). Multifunctional fibers for simultaneous optical, electrical and chemical interrogation of neural circuits in vivo. *Nat. Biotechnol.* **33**, 277.
57. Park, S., Guo, Y.Y., Jia, X.T., Choe, H.K., Grena, B., Kang, J., Park, J., Lu, C., Canales, A., Chen, R., et al. (2017). One-step optogenetics with multifunctional flexible polymer fibers. *Nat. Neurosci.* **20**, 612–619.
58. Wang, L.V. (2008). Tutorial on photoacoustic microscopy and computed tomography. *IEEE J. Selected Top. Quan. Electron.* **14**, 171–178.
59. Yoo, S., Park, J.H., and Nam, Y. (2019). Single-cell photothermal neuromodulation for functional mapping of neural networks. *ACS Nano* **13**, 544–551.
60. Paviolo, C., Haycock, J.W., Cadusch, P.J., McArthur, S.L., and Stoddart, P.R. (2014). Laser exposure of gold nanorods can induce intracellular calcium transients. *J. Biophotonics* **7**, 761–765.
61. de Boer, W.D.A.M., Hirtz, J.J., Capretti, A., Gregorkiewicz, T., Izquierdo-Serra, M., Han, S., Dupre, C., Shymkiv, Y., and Yuste, R. (2018). Neuronal photoactivation through second-harmonic near-infrared absorption by gold nanoparticles. *Light Sci. Appl.* **7**, 100.
62. Lee, J.W., Jung, H., Cho, H.H., Lee, J.H., and Nam, Y. (2018). Gold nanostar-mediated neural activity control using plasmonic photothermal effects. *Biomaterials* **153**, 59–69.
63. Lee, J.W., Kang, H., and Nam, Y. (2018). Thermo-plasmonic gold nanofilms for simple and mass-producible photothermal neural interfaces. *Nanoscale* **10**, 9226–9235.
64. Shibasaki, K., Suzuki, M., Mizuno, A., and Tominaga, M. (2007). Effects of body temperature on neural activity in the hippocampus: regulation of resting membrane potentials by transient receptor potential vanilloid 4. *J. Neurosci.* **27**, 1566–1575.
65. Kamimura, H.A.S., Conti, A., Toschi, N., and Konofagou, E.J.F.I.P. (2020). Ultrasound neuromodulation: mechanisms and the potential of multi-modal stimulation for neuronal function assessment. *Front. Phys.* **8**, 150.
66. Tyler, W.J., Lani, S.W., and Hwang, G.M. (2018). Ultrasonic modulation of neural circuit activity. *Curr. Opin. Neurobiol.* **50**, 222–231.
67. Kubanek, J., Shi, J., Marsh, J., Chen, D., Deng, C., and Cui, J. (2016). Ultrasound modulates ion channel currents. *Sci. Rep.* **6**, <https://doi.org/10.1038/srep24170>.
68. Kubanek, J., Shukla, P., Das, A., Baccus, S.A., and Goodman, M.B. (2018). Ultrasound elicits behavioral responses through mechanical effects on neurons and ion channels in a simple nervous system. *J. Neurosci.* **38**, 3081–3091.
69. Yoo, S., Mittelstein, D.R., Hurt, R.C., Lacroix, J.J., and Shapiro, M.G. (2020). Focused ultrasound excites neurons via mechanosensitive calcium accumulation and ion channel amplification. *bioRxiv*. <https://doi.org/10.1101/2020.05.19.101196>.
70. Maignret, F., Fosset, M., Lesage, F., Lazdunski, M., and Honoré, E. (1999). TRAAK is a mammalian neuronal mechano-gated K⁺ channel. *J. Biol. Chem.* **274**, 1381–1387.
71. Coste, B., Mathur, J., Schmidt, M., Earley, T.J., Ranade, S., Petrus, M.J., Dubin, A.E., and Patapoutian, A. (2010). Piezo1 and Piezo2 are essential components of distinct mechanically activated cation channels. *Science* **330**, 55–60.
72. Kang, L., Gao, J., Schafer, W.R., Xie, Z., and Xu, X.Z.S. (2010). *C. elegans* TRP family protein TRP-4 is a pore-forming subunit of a native mechanotransduction channel. *Neuron* **67**, 381–391.
73. Bagriantsev, S.N., Gracheva, E.O., and Gallagher, P.G. (2014). Piezo proteins: regulators of mechanosensation and other cellular processes. *J. Biol. Chem.* **289**, 31673–31681.
74. Brohawn, S.G., Campbell, E.B., and MacKinnon, R. (2014). Physical mechanism for gating and mechanosensitivity of the human TRAAK K⁺ channel. *Nature* **516**, 126–130.
75. Brohawn, S.G., Su, Z., and MacKinnon, R. (2014). Mechanosensitivity is mediated directly by the lipid membrane in TRAAK and TREK1 K⁺ channels. *Proc. Natl. Acad. Sci. U S A* **111**, 3614–3619.
76. Shi, L., Jiang, Y., Zhang, Y., Lan, L., Huang, Y., Cheng, J.-X., and Yang, C. (2020). A fiber optoacoustic emitter with controlled ultrasound frequency for cell membrane sonoporation at submillimeter spatial resolution. *Photoacoustics*, 100208.
77. Lin, C.-R., Chen, K.-H., Yang, C.-H., Cheng, J.-T., Sheen-Chen, S.-M., Wu, C.-H., Sy, W.-D., and Chen, Y.-S. (2010). Sonoporation-mediated gene transfer into adult rat dorsal root ganglion cells. *J. Biomed. Sci.* **17**, 44.
78. Krasovitski, B., Frenkel, V., Shoham, S., and Kimmel, E. (2011). Intramembrane cavitation as a unifying mechanism for ultrasound-induced bioeffects. *Proc. Natl. Acad. Sci. U S A* **108**, 3258–3263.
79. Plaksin, M., Shoham, S., and Kimmel, E. (2014). Intramembrane cavitation as a predictive bio-piezoelectric mechanism for ultrasonic brain stimulation. *Phys. Rev. X* **4**, 011004.
80. Wu, D., Huang, L., Jiang, M.S., and Jiang, H. (2014). Contrast agents for photoacoustic and thermoacoustic imaging: a review. *Int. J. Mol. Sci.* **15**, 23616–23639.
81. Miao, Q., Xie, C., Zhen, X., Lyu, Y., Duan, H., Liu, X., Jokerst, J.V., and Pu, K. (2017). Molecular afterglow imaging with bright, biodegradable polymer nanoparticles. *Adv. Mater.* **35**, 1102.
82. Lyu, Y., He, S., Li, J., Jiang, Y., Sun, H., Miao, Y., and Pu, K. (2019). A photolabile semiconducting polymer nanotransducer for near-infrared regulation of CRISPR/Cas9 gene editing. *Angew. Chem. Int. Ed.* **58**, 18197–18201.
83. Koirala, M., Sarma, R., Cao, H., and Yamilov, A. (2019). Inverse design of long-range intensity correlation in scattering media. *Phys. Rev. B* **100**, <https://doi.org/10.1103/PhysRevB.100.064203>.
84. Yamilov, A.G., Sarma, R., Redding, B., Payne, B., Noh, H., and Cao, H. (2014). Position-dependent diffusion of light in disordered waveguides. *Phys. Rev. Lett.* **112**, <https://doi.org/10.1103/PhysRevLett.112.023904>.
85. Chen, X., Zhang, C., Lin, P., Huang, K.C., Liang, J., Tian, J., and Cheng, J.X. (2017). Volumetric chemical imaging by stimulated Raman projection microscopy and tomography. *Nat. Commun.* **8**, 15117.
86. Ao, Y., Zeng, K., Yu, B., Miao, Y., Hung, W., Yu, Z., Xue, Y., Tan, T.T.Y., Xu, T., and Zhen, M. (2019). An upconversion nanoparticle enables near infrared-optogenetic manipulation of the *Caenorhabditis elegans* motor circuit. *ACS Nano* **13**, 3373–3386.
87. All, A.H., Zeng, X., Teh, D.B.L., Yi, Z., Prasad, A., Ishizuka, T., Thakor, N., Hiromu, Y., and Liu, X. (2019). Expanding the toolbox of upconversion nanoparticles for in vivo optogenetics and neuromodulation. *Adv. Mater.* **31**, 1803474.
88. Yu, N., Huang, L., Zhou, Y., Xue, T., Chen, Z., and Han, G. (2019). Near-infrared-light activatable nanoparticles for deep-tissue-penetrating wireless optogenetics. *Adv. Healthc. Mater.* **8**, 1801132.
89. Chen, S., Weitmier, A.Z., Zeng, X., He, L., Wang, X., Tao, Y., Huang, A.J., Hashimoto-dani, Y., Kano, M., and Iwasaki, H. (2018). Near-infrared deep brain stimulation via upconversion nanoparticle-mediated optogenetics. *Science* **359**, 679–684.
90. Yoo, S., Park, J.-H., and Nam, Y. (2018). Single-cell photothermal neuromodulation for functional mapping of neural networks. *ACS Nano* **13**, 544–551.
91. Aryal, M., Papademetriou, J., Zhang, Y.-Z., Power, C., McDannold, N., and Porter, T. (2016). Ultrasound-mediated delivery of gadolinium and fluorescent-labeled liposomes through the blood-brain barrier. *J. Acoust. Soc. Am.* **139**, 2093.
92. Aryal, M., Papademetriou, I., Zhang, Y.Z., Power, C., McDannold, N., and Porter, T. (2019). MRI monitoring and quantification of ultrasound-mediated delivery of liposomes dually labeled with gadolinium and fluorophore through the blood-brain barrier. *Ultrasound Med. Biol.* **45**, 1733–1742.
93. Zhang, W., Tong, L., and Yang, C. (2012). Cellular binding and internalization of functionalized silicon nanowires. *Nano Lett.* **12**, 1002–1006.
94. Jain, P.K., Lee, K.S., El-Sayed, I.H., and El-Sayed, M.A. (2006). Calculated absorption and scattering properties of gold nanoparticles of different size, shape, and composition: applications in biological imaging and biomedicine. *J. Phys. Chem. B* **110**, 7238–7248.
95. Cook, J.R., Bouchard, R.R., and Emelianov, S.Y. (2011). Tissue-mimicking phantoms for photoacoustic and ultrasonic imaging. *Biomed. Opt. Express* **2**, 3193–3206.